Supplementary Information

Tricycloquinazoline Based 2D Conjugated Metal-Organic Framework for Robust Sodium-Ion Batteries with Ion Co-Storage of Both Cations and Anions

Dan Chen[‡,a,c], Linqi Cheng[‡,d], Weiben Chen[‡,a,c] , Heng-Guo Wang[b,*], Fengchao Cui[b], and Long Chen[a,*]

[a]*State Key Laboratory of Supramolecular Structure and Materials, College of Chemistry, Jilin University, Changchun 130012, China.*

[b]*Key Laboratory of Polyoxometalate and Reticular Material Chemistry of Ministry of Education, Faculty of Chemistry, Northeast Normal University, Changchun 130024, China.*

[c]*Department of Chemistry, Tianjin Key Laboratory of Molecular Optoelectronic Science, Tianjin University, Tianjin, 300072, China.*

[‡]*These authors contributed equally: Dan Chen, Linqi Cheng, and Weiben Chen.*

E-mail: longchen@jlu.edu.cn, wanghg061@nenu.edu.cn.

Section 1. Materials and Methods

All raw materials were purchased from Shanghai Bepharm Science&Technology Co., Ltd. and Shanghai Titan Scientific Co., Ltd. Furthermore, all of commercial chemical compounds were used directly without further purification and the solvents were dried according to standard methods.

^{1}H NMR and ^{13}C NMR of all monomers were recorded on Bruker AVANCE III-400MHz NMR spectrometer. The powder X-ray diffraction (PXRD, 9 KW) patterns were recorded on X-ray diffractometer (RIGAKU SMARTLAB9KW) with a Cu-target tube and a graphite monochromator. Fourier transform infrared (FT-IR) spectroscopies were done on a Bruker ALPHA spectrometer in the range of 400-4000 cm^{-1}. X-ray photoelectron spectroscopy (XPS) was measured on a Thermo Scientific K-Alpha. The X-ray absorption fine structure (XAFS) spectrum was collected at the XRD station of beamline 4B9A of Beijing Synchrotron Radiation Facility (BSRF). The Ni K edge (8333 eV) was measured on a bending magnet beam line. The experiments were performed in transmission mode with argon and N$_2$-filled ionization chambers. The Athena was used to normalize and calibrate the data and Artemis was used to simulate spectra of model structures determined by density functional theory. HamaFortran was used to calculate the wavelet transform of extended X-ray absorption fine structure (EXAFS) spectra. High-resolution transmission electron microscopies (HR-TEM) were performed on JEOL model JSM-2100F. Field-emission scanning electron microscopies (FE-SEM) were performed on a Hitachi SU8010 microscope operating at an accelerating voltage of 5.0 kV. UV-vis diffuse reflectance spectra (Kubelka-Munk-transformed reflectance spectra) were measured on PerkinElmer Lambda 750 spectrophotometer. Elemental analysis was measured by Elementar Vario EL III to obtain content of C, H, N. ICP-OES/MS was measured by Agilent 5110 to obtain content of Ni element. Thermogravimetric analysis of Ni$_3$(HATQ)$_2$ was evaluated via using a differential thermal analysis instrument (TA instruments TGA-Q50-1918 analyzer) ranging from room temperature to 800 °C with the interval of 10 °C min^{-1} under N$_2$ atmosphere. Specific surface areas and pore size distribution were measured via Bel Japan Inc. model BELSOPR-mini II analyzer by drying samples at 85 °C for 8 hours under vacuum (10^{-5} bar), and pore size distribution was calculated by nonlocal density functional theory (NLDFT). The Ni$_3$(HATQ)$_2$ structure was simulated using a hexagonal unit cell in Material Studio 2017 package. The resulted structure was pre-optimized in Forcite calculation modulation and further optimized by using density functional tight-binding (DFTB+) method.

Electrochemical measurements: The CR2025 coin-type half batteries were assembled in an Ar-filled glove box. The electrode pellet was prepared by casting the mixture of 60 wt% Ni$_3$(HATQ)$_2$, 30 wt% acetylene black, and 10 wt% polyvinylidene fluoride (PVDF) in anhydrous NMP onto an Al foil (for cathode), followed by drying at 100 °C in vacuum for 12 h. Next, sodium metal was used as the reference electrode, 1.0 M NaPF$_6$ dissolved in DME (120 μL) were used as electrolyte and fiberglass was used as the separator. The thickness of electrode plate is 20 μm and areal mass loading of active material on current collector is 1.0 mg cm^{-2}. The electrochemical performance of Ni$_3$(HATQ)$_2$ electrodes including galvanostatic charge/discharge (GCD), cyclic voltammetry (CV) and electrochemical impedance spectroscopy (EIS) tests were evaluated in CR2025-type coin cells at room temperature. CV measurements were tested by CHI600E electrochemical workstation with the voltage range of 1.0-3.6 V. Electrochemical measurements were evaluated by the NEWARE battery system. The chemical diffusion coefficient of Na$^+$ ions was tested by galvanostatic intermittent titration technique (GITT) at a current density of 0.05 A g^{-1} for 10 min followed by 30 min of relaxation. $D_S =4/\pi\tau*((n_mVm)/S)^2*(\Delta E_S/\Delta E_t)^2$, τ is a relaxation time; n$_m$ is the number of moles, and the Vm is the molar volume of the electrode material, and S is an electrode contact area, and ΔE_s is a voltage change caused by pulses, ΔE_t is the voltage change of constant current charge and discharge.

Coin-type full cell: the electrode pellet was prepared by casting the mixture of 60 wt% sodium terephthalate, 30 wt% acetylene black and 10 wt% PVDF in anhydrous NMP onto a Cu foil (for anode and undergoes a process of sodiation), 60 wt% MOF, 30 wt% acetylene black and 10 wt% PVDF in anhydrous NMP onto an Al foil (for cathode), followed by drying at 80 °C in vacuum for 12 h. Next, 1 M NaPF$_6$ dissolved in DME was used as electrolyte and fiberglass was used as the separator. The CR2025 coin-type batteries were assembled in an Ar-filled glove box. Electrochemical measurements were evaluated by the NEWARE battery system.

Computational details: All density functional theory (DFT) simulations were implemented in the Vienna Ab initio Simulation Package (VASP). Projector augmented wave (PAW) method was employed to describe core-valence interaction with plane wave cut-off energy of 500 eV. The generalized gradient approximation with the Perdew-Burke-Ernzerhof functional (GGA-PBE) was used to describe

the exchange-correlation potential of the electrons. Spin polarization calculations was performed for all simulations with the consideration of empirical dispersions of Grimme (DFT-D3) for the long-range vdW interactions. The Brillouin zone was sampled with the gamma centered Monkhorst-Pack k-point grid: a $1 \times 1 \times 9$ k-point grid for the systems. The convergence criterion of energy and structural relaxation were 1.0×10^{-6} eV and 0.01 eV/Å, respectively.

Calculation of Capacitive Contribution: The active material's voltammetric response and sweep rates can be described as follows[S1]:

$$i = av^b \tag{1}$$

$$logi = b * logv + loga \tag{2}$$

where i is peak current, v is sweep rate, a and b are constants. When the value of slope b is close to 0.5, it means existence of Na$^+$ diffusion-controlled process, meanwhile, the process is dominated by capacitive effect when b approaches to 1[S2].

To further quantitatively determine the capacitive contribution by current response according to Dunn equation[S3]:

$$i(V) = k_1v + k_2v^{1/2} \tag{3}$$

where k_1 and k_2 are adjustable parameters. At a fixed potential, the current response i (V) can be separated into surface capacitive (k_1v) and diffusion-controlled ($k_2v^{1/2}$) contribution.

Section 2. Synthetic Procedures
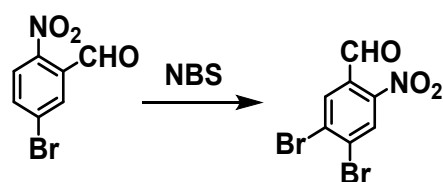
Scheme S1: 4,5-dibromo-2-nitrobenzaldehyde[S4].

In a 25 mL single-necked flask, 5-bromo-2-nitrobenzaldehyde (400 mg, 1.74 mmol) was added to 6 mL 98% H$_2$SO$_4$ and stirred, then *N*-bromosuccinimide (NBS, 780 mg, 4.39 mmol) was added stepwise into the reaction mixture, then the reaction mixture was stirred at room temperature for 24 h. The reaction mixture was then poured into ice water and the resulted precipitate was collected by filtration under vacuum and purified by column chromatography with the eluent of petroleum ether. Finally, the product was obtained via rotary evaporation as a white powder (452 mg, 1.46 mmol, Yield = 84%). ^{1}H NMR (CDCl$_3$, 400 MHz) δ (ppm) = 8.19 (s, 1H), 8.39 (s, 1H), 10.39 (s, 1H).
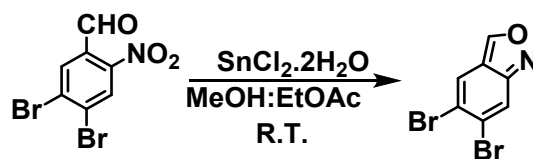
**Scheme S2.** Synthetic route of 5,6-dibromobenzo[c]isoxazole[S5,S6].

In a 50 mL single-necked flask, 4,5-dibromo-2-nitrobenzaldehyde (200 mg, 0.65 mmol) was dissolved in a mixed solvent of ethyl acetate and methanol (v:v = 1:1, 6 mL), then SnCl$_2$·2H$_2$O (446 mg, 1.95 mmol) was added to the mixture and kept reaction for 24 h at room temperature. The reaction mixture was quenched by saturated aqueous sodium bicarbonate solution (10 mL) and filtered. The aqueous phase was washed and extracted by ethyl acetate. The organic phase was concentrated by rotary evaporation and purified by column chromatography with the eluent of petroleum ether. The product was obtained as a white powder (120 mg, 0.43 mmol, Yield = 67%). ^{1}H NMR (CDCl$_3$, 400 MHz) δ (ppm) = 7.98 (s, 1H), 8.06 (s, 1H), 9.13 (s, 1H), ^{13}C NMR (CDCl$_3$, 100 MHz) δ (ppm): 118.12, 119.54, 121.06, 123.48, 128.47, 154.57, and 155.34.
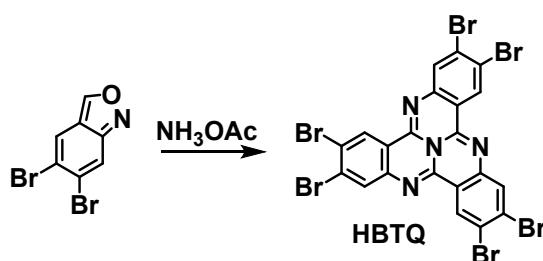
Scheme 3. Synthetic route of 2,3,7,8,12,13-hexabromo-4b^1,5,10,15-tetraazanaphtho[1,2,3-gh]tetraphene (**HBTQ**)[S5].

In a 50 mL two-necked flask, 5,6-dibromobenzo[c]isoxazole (60 mg, 0.22 mmol) and NH$_4$OAc (108 mg, 1.40 mmol) was mixed with

sulfone (2 mL) and AcOH (1 mL), the mixture was stirred at 150 °C for 16 h. After being cooled to room temperature, the reaction mixture was filtered and washed by ethanol. The green solid was collected and dried in vacuum (32 mg, 0.04 mmol, Yield = 55%). ^{1}H NMR (CDCl$_3$, CF$_3$COOH, 400 MHz) δ (ppm) = 8.12 (s, 3H), 8.84 (s, 3H).
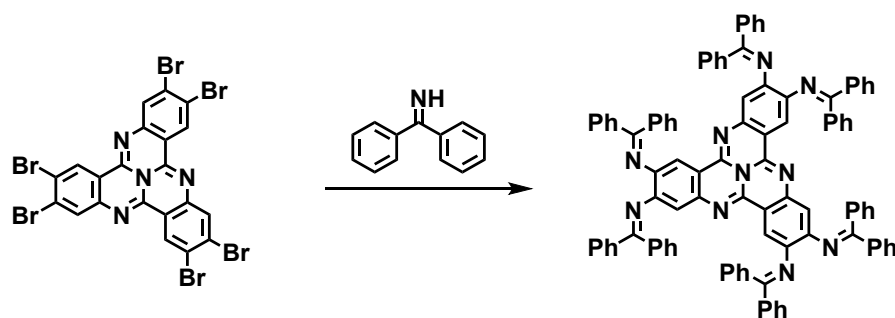

Scheme S4. Synthetic route of $N,N',N'',N''',N'''',N'''''$-(4b^1,5,10,15-tetraazanaphtho[1,2,3-gh]tetraphene-2,3,7,8,12,13-hexayl)hexakis(1,1-diphenylmethanimine)[S7].

Pd$_2$(dba)$_3$ (29.55 mg, 0.03 mmol) and *rac*-BINAP (52.51 mg, 0.08 mmol) was mixed in toluene (10 mL) and stirred at 110 °C for 30 min. After cooling to room temperature, 2,3,7,8,12,13-hexabromo-4b^1,5,10,15-tetraazanaphtho[1,2,3-gh]tetraphene (150 mg, 0.19 mmol), sodium *tert*-butoxide (546.75 mg, 5.69 mmol) and diphenylmethanimine (275.48 mL, 1.64 mmol) was sequentially added to the reaction mixture and stirred at 110 °C overnight. The reaction mixture was cooled to room temperature and filter via celatom and washed with dichloromethane and concentrated under vacuum. The crude product was purified by column chromatography with the eluent of dichloromethane/ethyl acetate (v:v=2:1) and collected as an orange powder (183 mg, 0.13 mmol, Yield = 70%). ^{1}H NMR (DMSO-d_6, 400 MHz) δ (ppm) = 6.34 (s, 3H), 7.11 (d, 6H, J = 8 Hz), 7.19 (s, 9H), 7.35 (d, 36H), 7.57 (s, 12H). ^{13}C NMR (DMSO-d_6, 100 MHz) δ (ppm): 115.59, 115.82, 128.59,128.88, 129.14, 129.31, 130.08, 131.21, 131.43, 136.25, 138.45, 138.95, 141.28, 141.45, 143.82, 149.62, 167.93, and 168.02. HR-MS (MALDI-TOF): Calcd. for C$_{99}$H$_{66}$N$_{10}$ m/z =1395.68700, [M+H]$^+$, found: m/z =1396.55725.
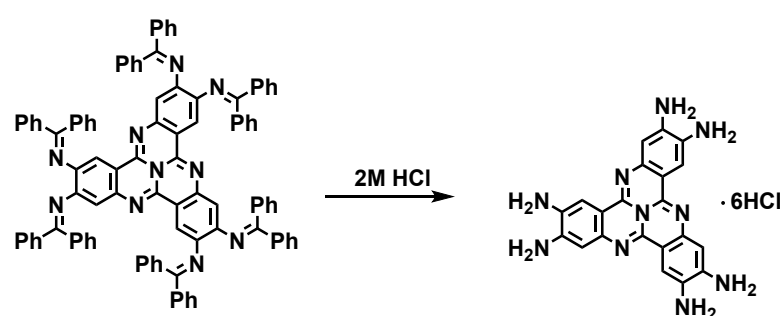
Scheme S5. Synthetic route of 4b^1,5,10,15-tetraazanaphtho[1,2,3-gh]tetraphene-2,3,7,8,12,13-hexaamine hexahydrochloride (denoted as **HATQ·6HCl**)[S7].

$N,N',N'',N''',N'''',N'''''$-(4b^1,5,10,15-tetraazanaphtho[1,2,3-gh]tetraphene-2,3,7,8,12,13-hexayl)hexakis(1,1-diphenylmethanimine) (500 mg, 0.11 mmol) was dissolved in tetrahydrofuran (18 mL), then 2M HCl (21 mL) was added to reaction and stirred for 4 h. The color of the reaction mixture turned from dark brown to yellow along with solid precipitation. The precipitated solid was collected by filtration and washed with tetrahydrofuran (192 mg, 0.08 mmol, Yield = 85%). The precipitated solid can be easily dissolved in water, indicating the hydrochloride salt formation. The contents of C, H, N of the precipitated solid measured by element analyses (EA) are 48.633%, 4.064%, 22.619%, respectively, which are close to the calculated contents of C (40,09%), H (3.84%), N (22.26%) of **HATQ·6HCl**. ^{1}H NMR (DMSO-d_6, 400 MHz) δ (ppm) = 6.74 (s, 6H), 7.68 (s,12H). ^{13}C NMR (DMSO-d_6, 100 MHz) δ (ppm): 106.63, 129.07, 130.08, 133.20, 141.95, 142.97, and 148.17. HR-MS (MALDI-TOF): Calcd. for C$_{21}$H$_{18}$N$_{10}$ m/z = 410.44500, [M+H]$^+$, found: m/z = 411.17892.
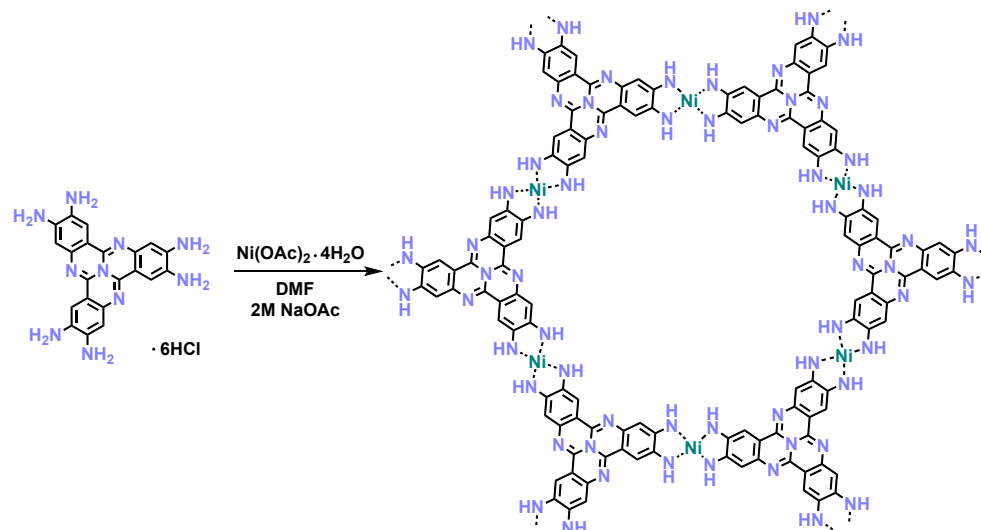

Scheme S6. Synthetic route of Ni$_3$(HATQ)$_2$.

A solution of nickel acetate (Ni(OAc)$_2$·4H$_2$O, 20.9 mg, 0.084 mmol) in water (7.2 mL) was added to a solution of **HATQ·6HCl** (35.56 mg, 0.056 mmol) in of *N,N*-dimethyformamide (DMF, 14.4 mL). The mixture was treated with ultrasonication for 10 min, then 0.8 mL aqueous AcONa (2 M) solution was added into the mixture and sonicated for another ten minutes. After ultrasonication, the reaction mixture was placed in a preheated oven (85 ℃) for 72 h. The resulted black solid was collected by filtration and thoroughly washed by water, methanol, DMF, *N,N*-dimethylacetamide (DMA) and acetone, and dried under vacuum at 85 ℃ overnight. Elemental analysis: Calcd. for Ni$_3$(HATQ)$_2$ (H$_2$O)$_3$ (DMF)$_3$: C, 48.69%; H, 4.09%; N, 25.60%; Ni, 13.99%. Found: C, 42.87%; H, 4.49%; N, 21.99%; Ni, 12.64%.
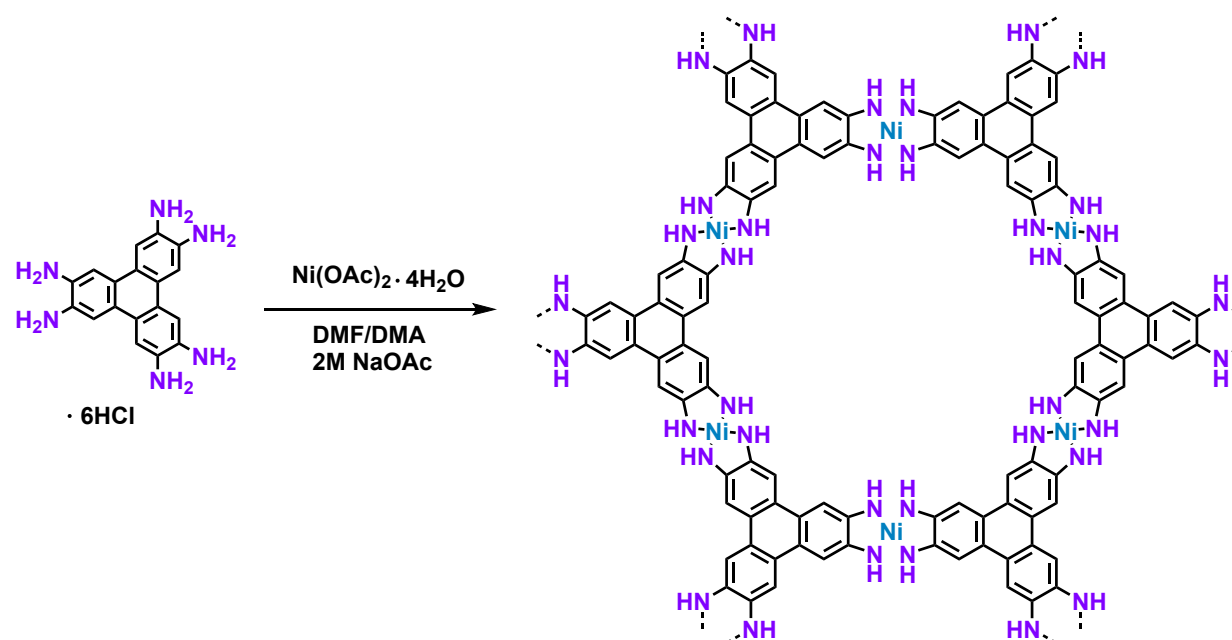
Scheme S7. Synthetic route of Ni$_3$(HITP)$_2$[S8].

A solution of Ni(OAc)$_2$·4H$_2$O (17.4 mg, 0.070 mmol) in DMF (15 mL) / DMA (15 mL) was preheated at 65 ℃. Then, 2M NaOAc aqueous solution (20 mL) and **HITP·6HCl** (HITP= hexaiminotriphenylene) (25 mg, 0.046 mmol) dissolved in water (7.5 mL) were added respectively. Afterwards, the mixture was stirred and heated at 65 ℃ for 2 h. After cooling to room temperature, the precipitation was filtered and washed by DMF, DMA, water and acetone. The black powder was dried under vacuum at 85 ℃ overnight.

Section 3. Structural Characterization of Monomers
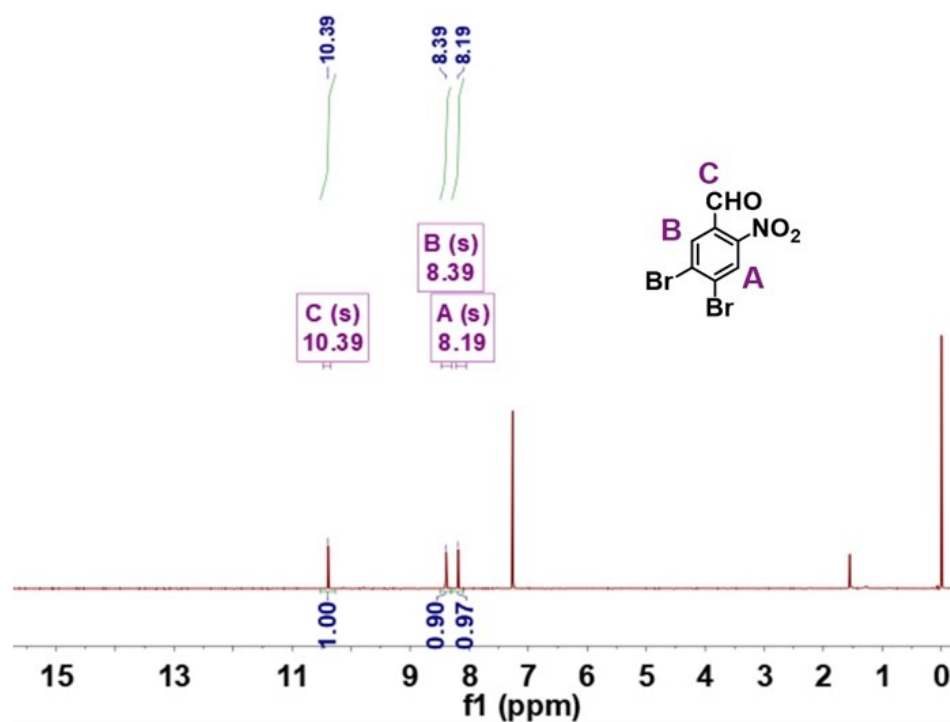
Fig. S1 ^{1}H NMR spectrum (400 MHz) of 4,5-dibromo-2-nitrobenzaldehyde in CDCl$_3$.
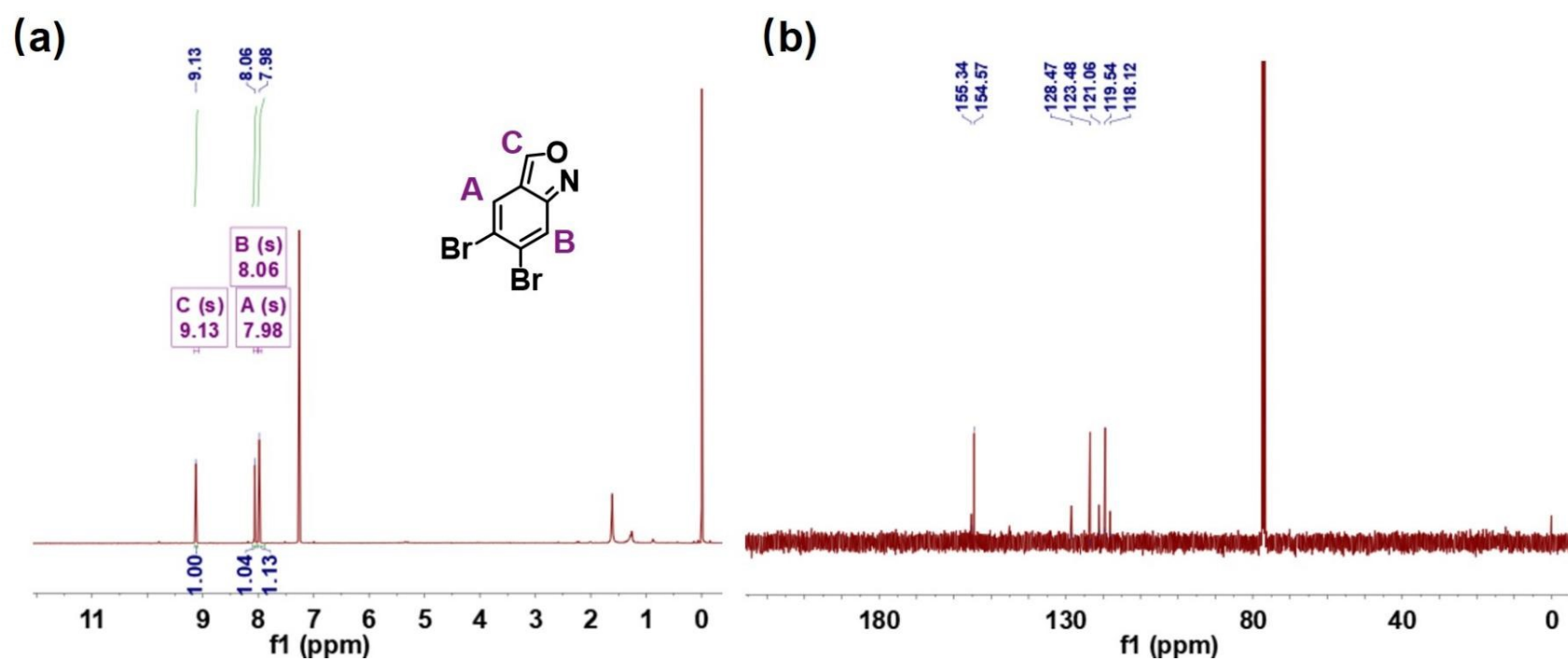
Fig. S2 ¹H NMR (400 MHz) and ¹³C NMR (100 MHz) spectra of 5,6-dibromobenzo[c]isoxazole in CDCl₃.
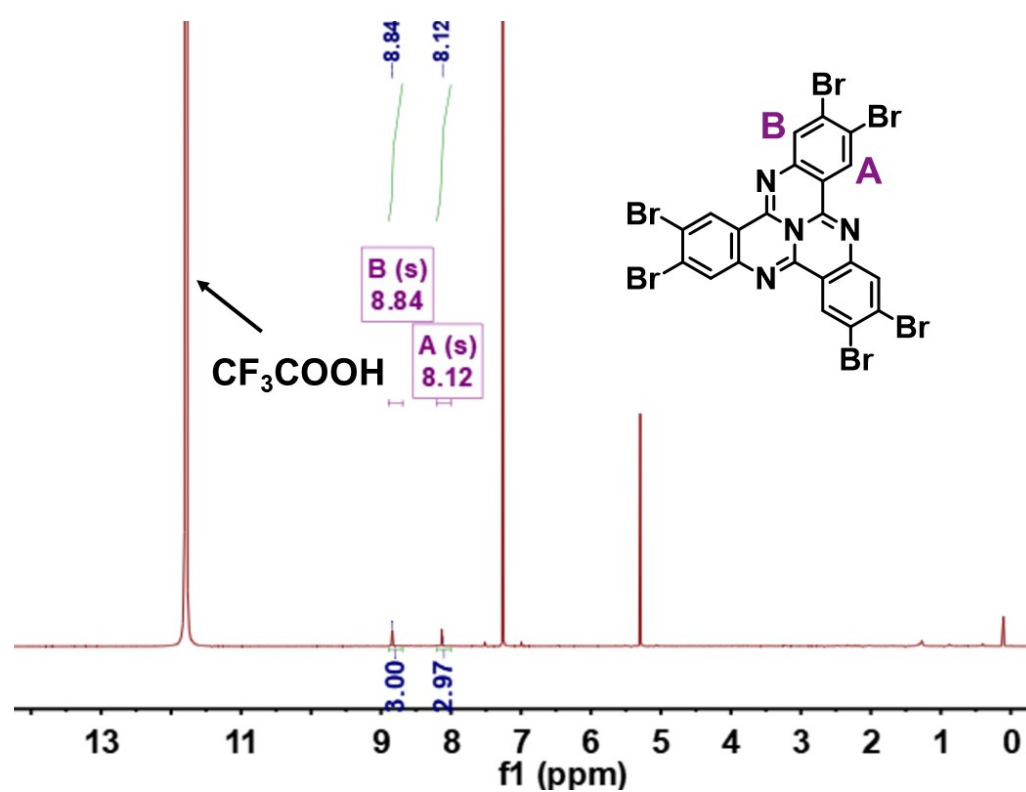
Fig. S3 ¹H NMR spectrum (400 MHz) of HBTQ in CDCl₃/CF₃COOH.
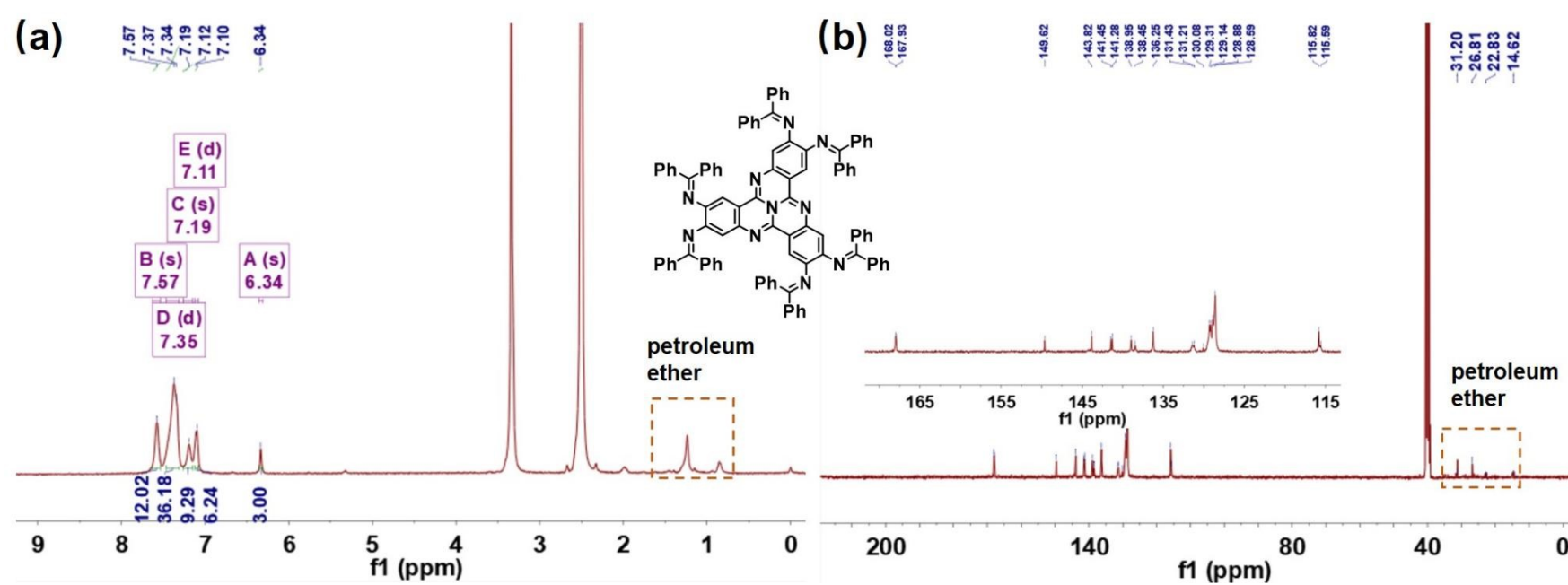
Fig. S4 ¹H NMR (400 MHz) and ¹³C NMR (100 MHz) spectra of *N,N′,N″,N‴,N⁗,N‴‴*-(4b¹,5,10,15-tetraazanaphtho[1,2,3-gh]tetraphene-2,3,7,8,12,13-hexayl)hexakis(1,1-diphenylmethanimine) in DMSO-*d₆*.
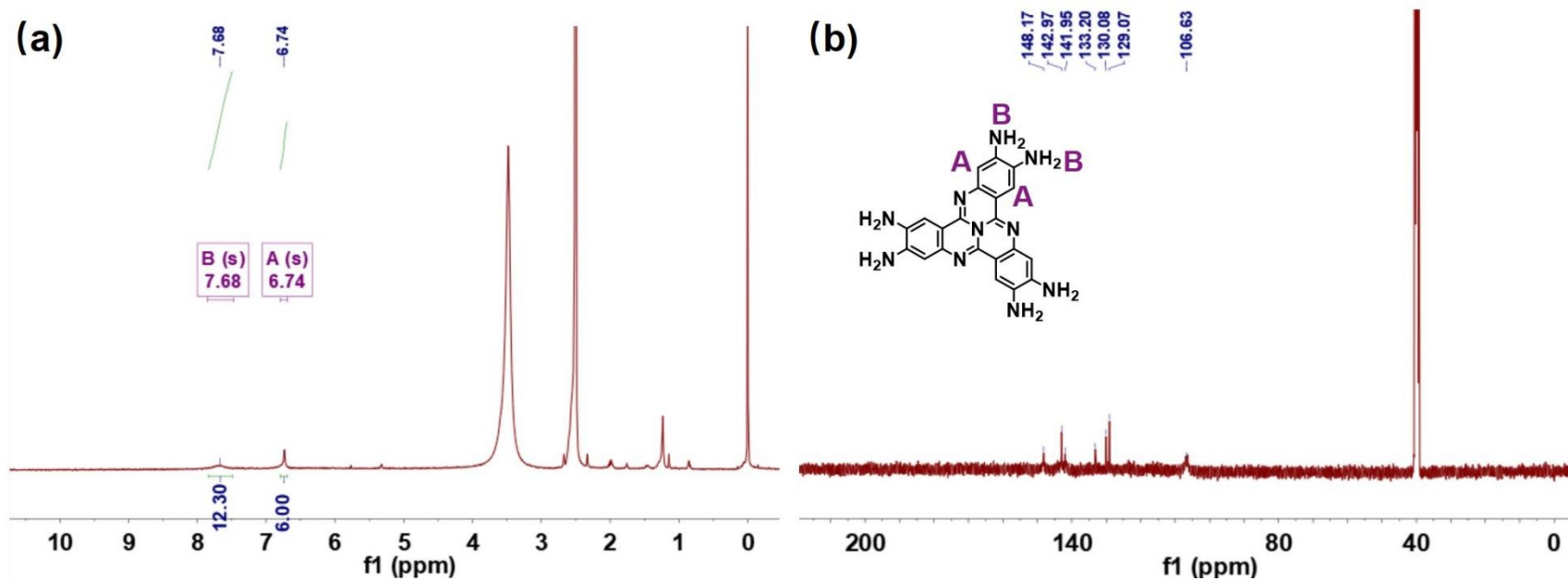
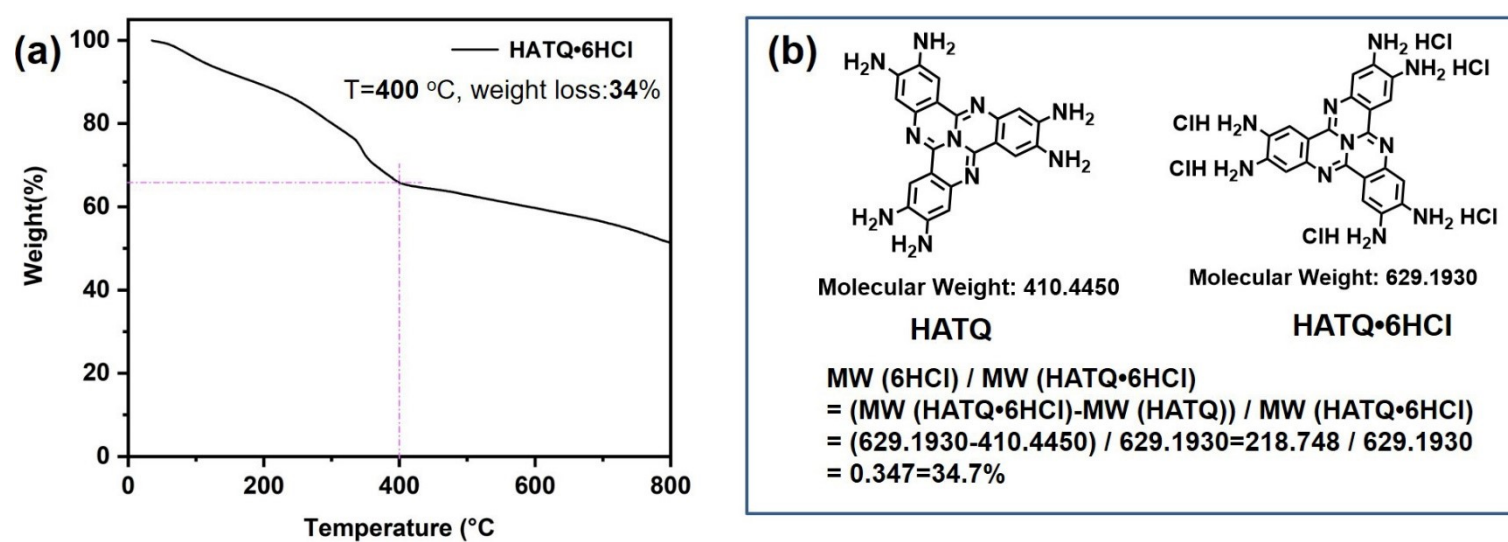**Fig. S5** ^{1}H NMR (400 MHz) and ^{13}C NMR (100 MHz) spectra of HATQ·6HCl in DMSO-d_6.
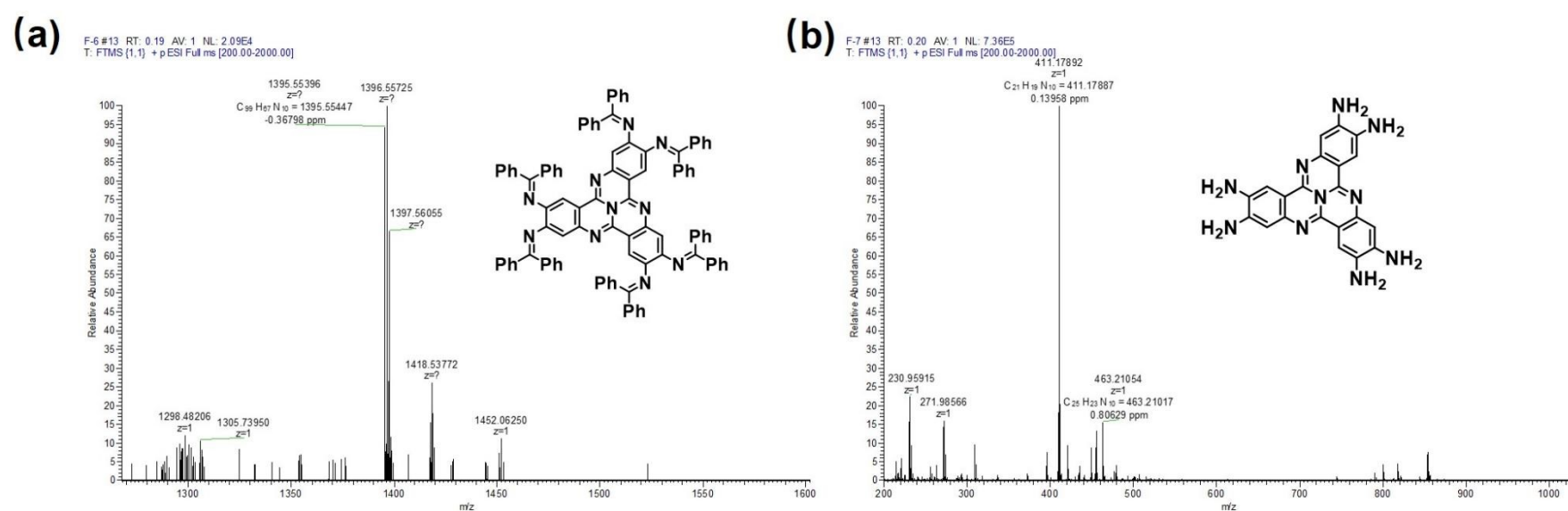
Fig. S6 High resolution mass spectra of $N,N',N'',N''',N'''',N'''''$-(4b[1],5,10,15-tetraazanaphtho[1,2,3-gh]tetraphene-2,3,7,8,12,13-hexayl)hexakis(1,1-diphenylmethanimine) and HATQ·6HCl.

Fig. S7 Thermogravimetric analysis (TGA) data of HATQ•6HCl measured from room temperature to 800 °C at 10 °C min^{-1}. As shown in Figure S7a, the 400 °C is turning point of the weight loss. The weight loss (34%) is fast before 400 °C, which is attributed to the weight loss of 6HCl in line with the calculated percentage (34.7%) of the mass of the six hydrochloric acids in the total mass. The weight loss is slow after 400 °C, corresponding to pyrogenic decomposition of HATQ.
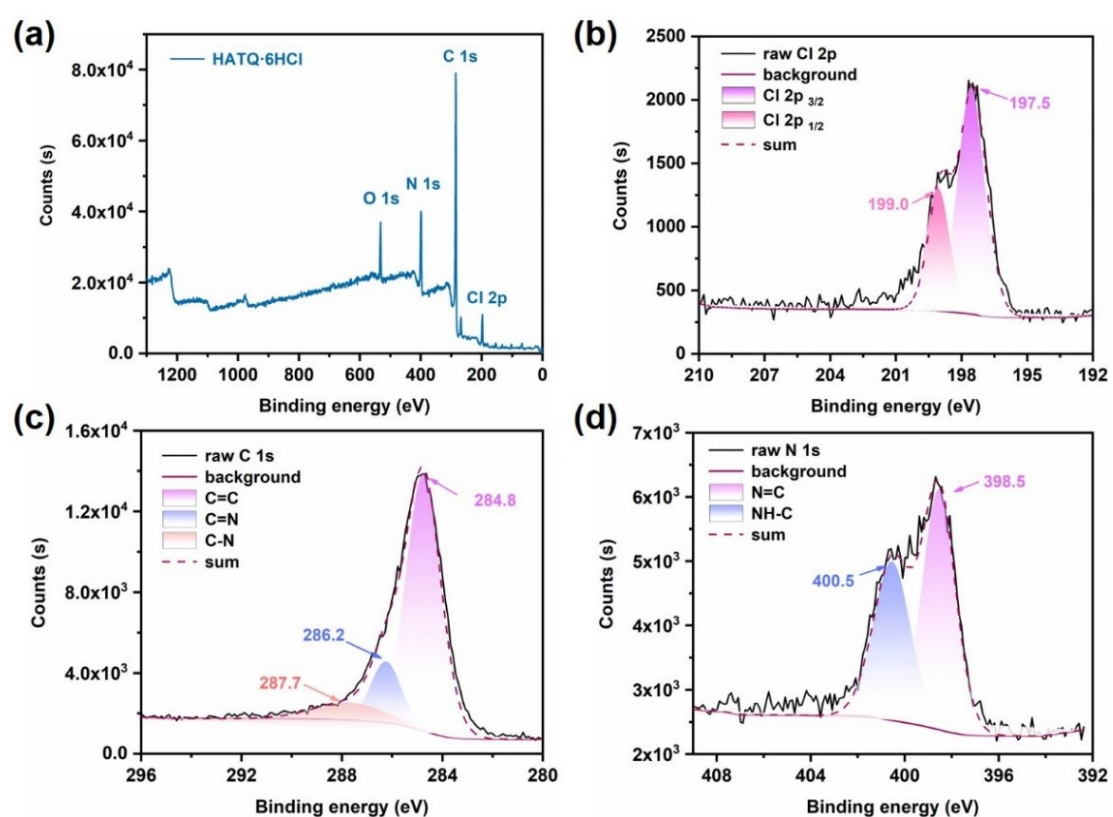
Fig. S8 (a) X-ray photoelectron spectroscopy (XPS) of full energy spectrum for all elements of HATQ·6HCl; (b) high resolution XPS Cl(2p) spectrum of HATQ·6HCl; (c) high resolution XPS C(1s) spectrum of HATQ·6HCl and (d) high resolution XPS N(1s) spectrum of HATQ·6HCl.

Section 4. The Reaction Condition Screening
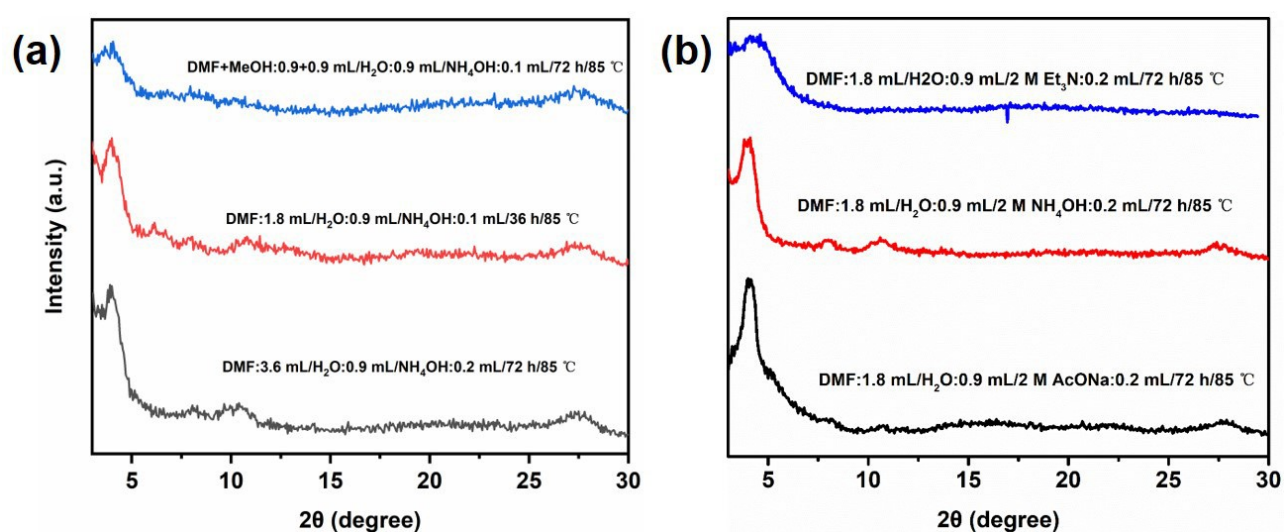
Fig. S9 PXRD profiles (data collected on DX-27 mini X-Ray diffractometer) of $Ni_3(HATQ)_2$ under (a) different solvents and (b) different base conditions. Owing to poor reproducibility in NH_4OH, the best condition for small attempts is 3.6 mL of DMF, 1.8 mL of H_2O and 0.2 mL of NaOAc at 85 °C for 72 h.

Section 5. Structural Characterization of $Ni_3(HATQ)_2$
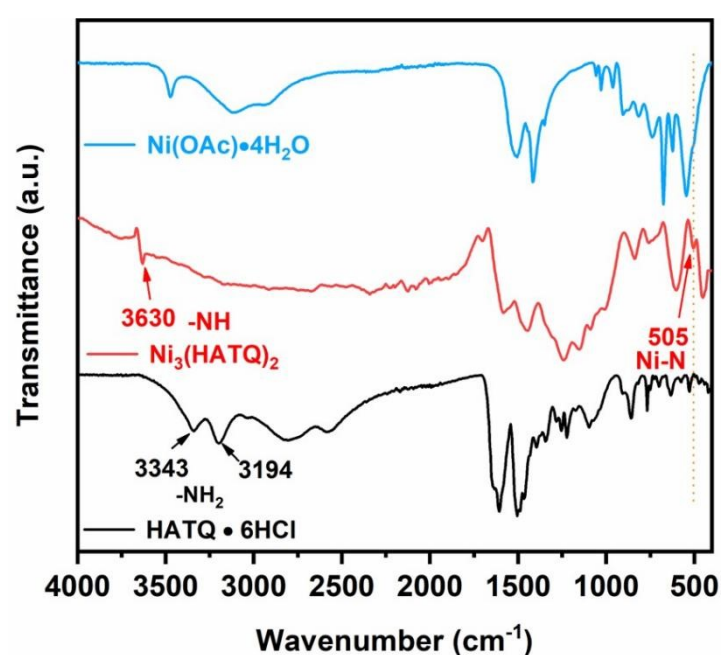
Fig. S10 FT-IR spectral profiles of $Ni_3(HATQ)_2$ compared with corresponding precursors.
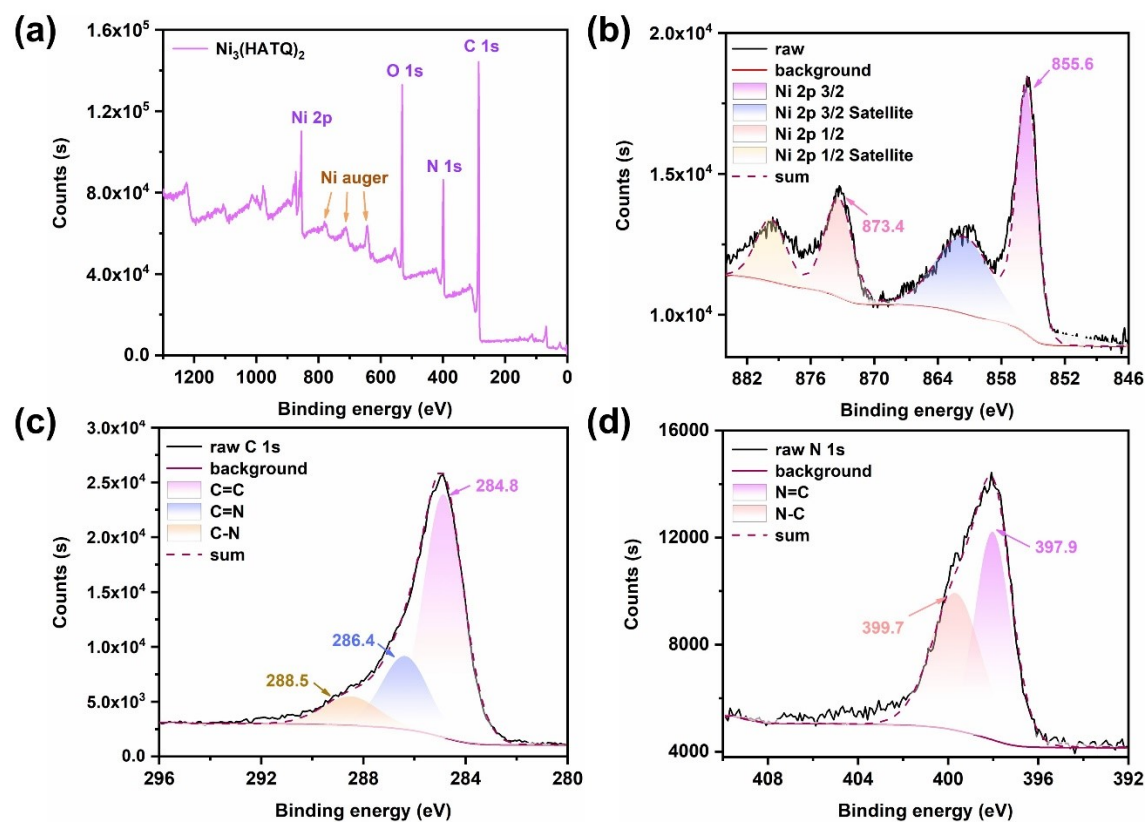
Fig. S11 (a) X-ray photoelectron spectroscopy (XPS) of full energy spectrum for all elements $Ni_3(HATQ)_2$; (b) high resolution XPS Ni(2p) spectrum of $Ni_3(HATQ)_2$; (c) high resolution XPS C(1s) spectrum of $Ni_3(HATQ)_2$ and (d) high resolution XPS N(1s) spectrum of $Ni_3(HATQ)_2$.
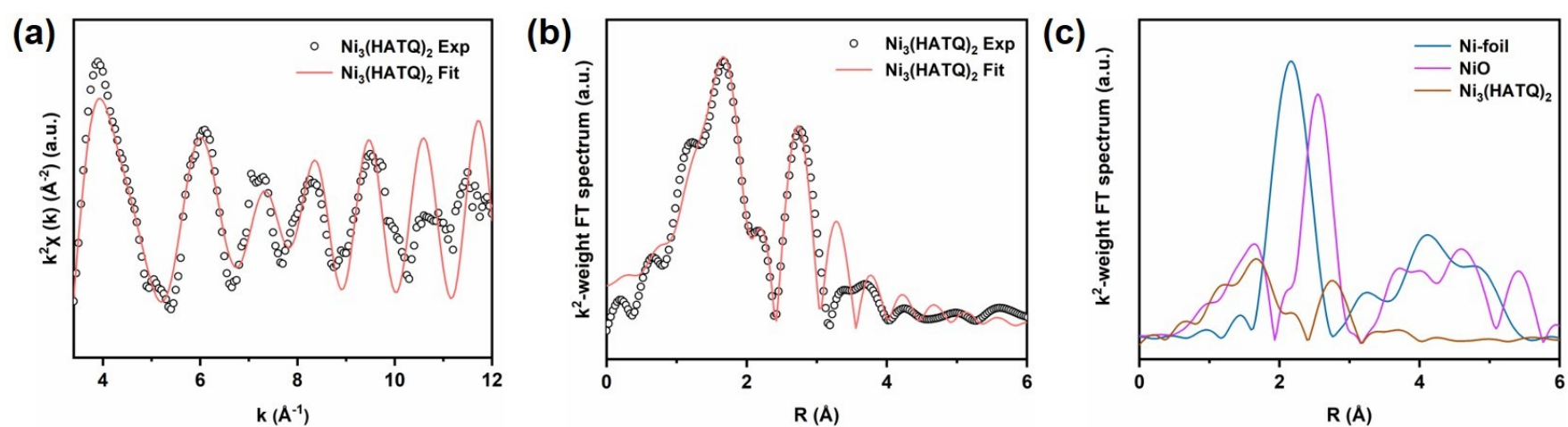

Fig. S12 (a) Ni K-edge extended X-ray absorption fine structure (EXAFS) oscillations $k^2\chi(k)$ in *k*-space and (b) its corresponding Fourier transform (FT) spectrum for sample $Ni_3(HATQ)_2$ in *R*-space; (c) Fourier transform (FT) spectrum comparisons of Ni K-edge EXAFS oscillations $k^2\chi(k)$ for $Ni_3(HATQ)_2$, NiO and Ni foil in *R*-space.
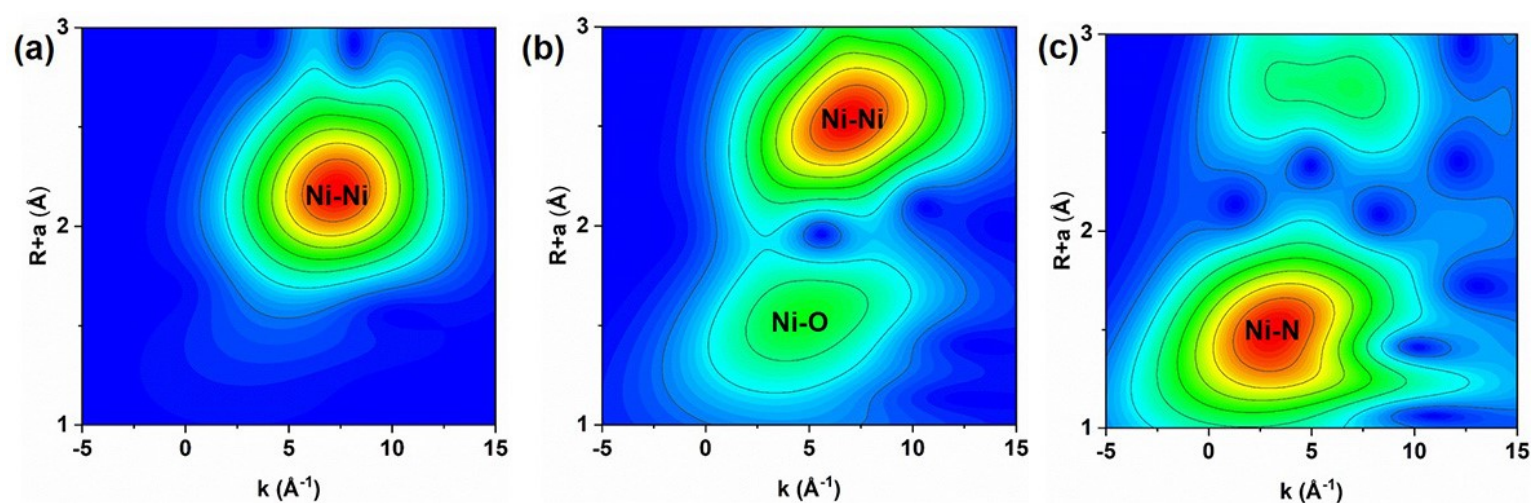
Fig. S13 The wavelet transforms EXAFS of (a) Ni foil, (b) Ni-O and (c) $Ni_3(HATQ)_2$. The wavelet transforms EXAFS (WT-EXAFS) spectra are used to visually investigate the coordination environment of Ni element in the $Ni_3(HATQ)_2$ and the reference samples (Ni foil/NiO) by providing *R*-space and *k*-space values in Figure S12c and S13, respectively. For the WT-EXAFS of standard Ni foil, the only peak of maximum intensity at *k*-space value of *ca.* 7.5 Å^{-1} and *R*-space value of *ca.* 2.2 Å can match well with the Ni-Ni bond. Differently, two distinct maximum intense peaks at *k*-space values of *ca.* 4.2 Å^{-1} (*R*-space value of *ca.* 1.6 Å) and *ca.* 5.8 Å^{-1} (*R*-space value of *ca.* 2.5 Å) are assigned to the Ni-O and Ni-Ni bonds, respectively. Obviously, the peak of maximum intensity at *k*-space value of *ca.* 3.3 Å^{-1} and *R*-space value of *ca.* 1.7 Å is ascribe to the Ni-N bonds without apparent intensity maximum of Ni-Ni bond, which indicates no residual metallic Ni in the $Ni_3(HATQ)_2$.

Table S1. Structure parameters (coordination numbers **n**, interatomic distances **R**, disorder factors **σ²**) of Ni₃(HATQ)₂ obtained in fitting of experimental Ni K-edge EXAFS data in Figure 11b.

|	Bond	R (Å)	n	σ^2 (Å²)	ΔE (eV）	R factor
Ni₃(HATQ)₂	Ni-N	2.12	4.5	0.020	10.28	0.015
	Ni…C	3.13	1.3	0.007	10.28	
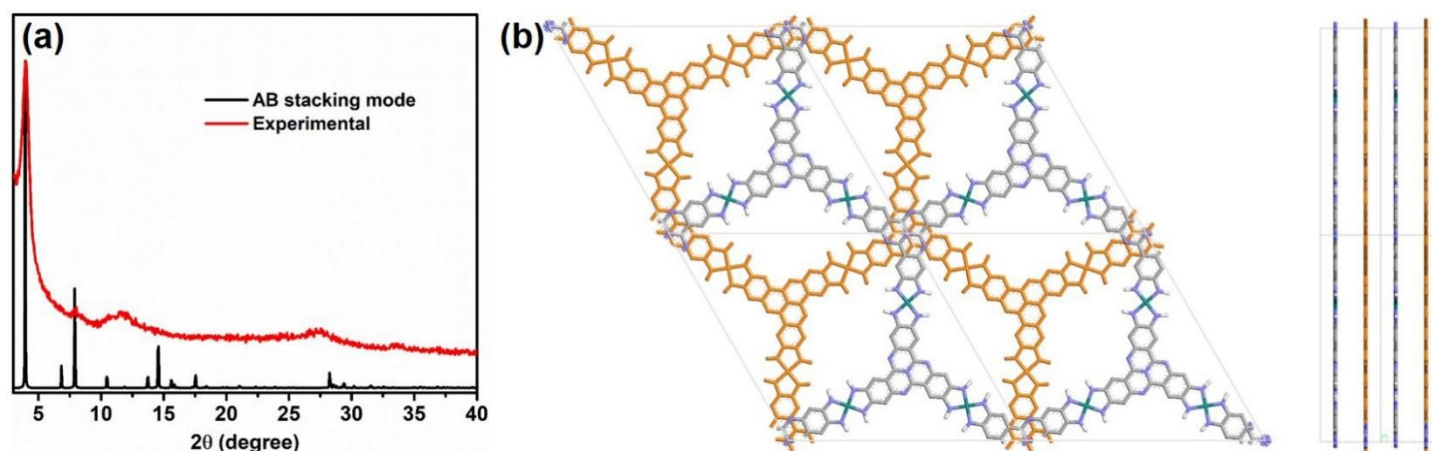
Fig. S14 (a) The experimental, simulated AB stacking of Ni₃(HATQ)₂; (b) top and side view of simulated AB stacking, respectively; the diffraction profile of the staggered AB stacking model cannot agree with the experimental data.
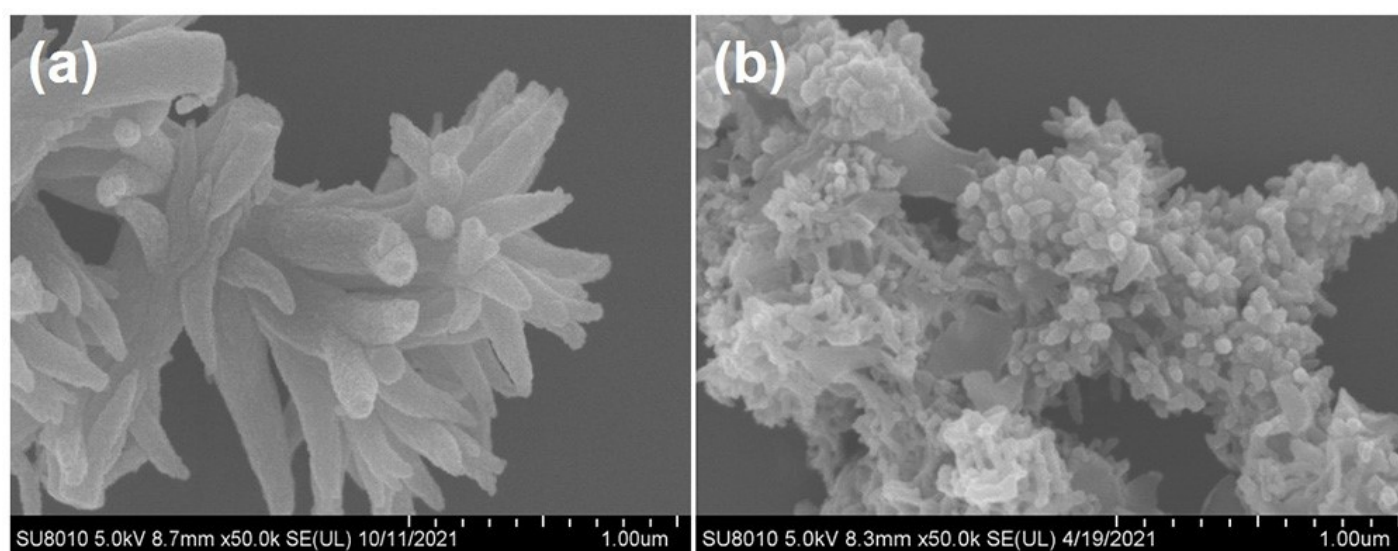
Fig. S15 Scanning electron microscopy (SEM) images of Ni₃(HATQ)₂ synthesized from (a) NaOAc and (b) NH₄OH.
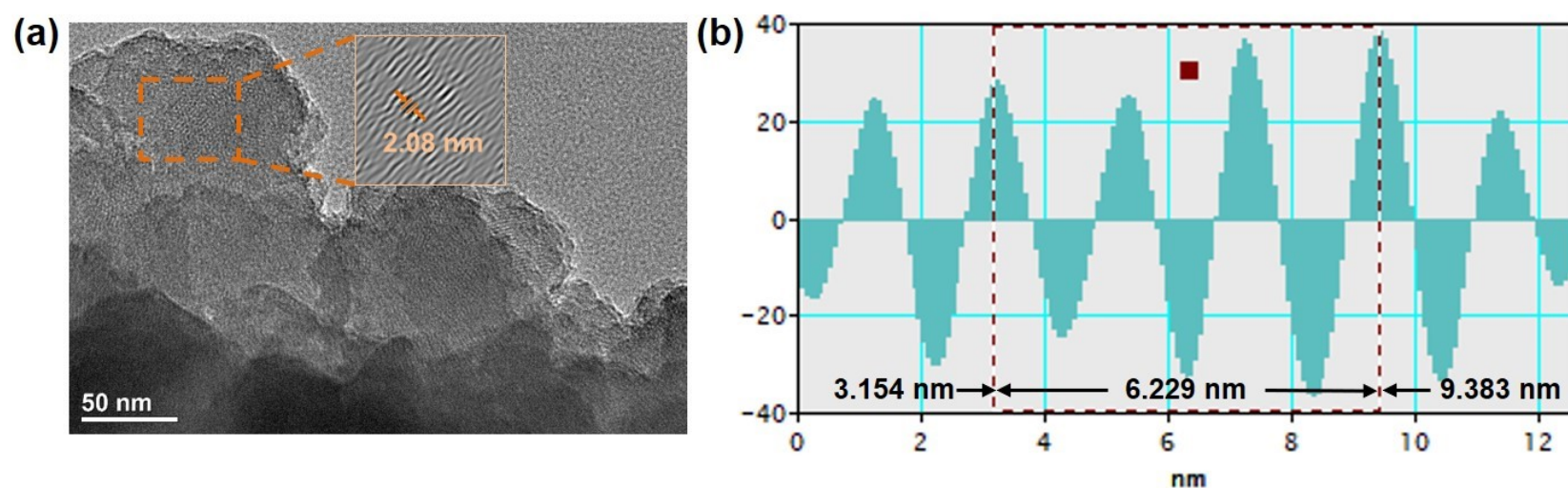
Fig. S16 (a) HR-TEM images of Ni₃(HATQ)₂. Inset shows the IFFT images calculated from corresponding TEM images. (b) d-spacing of Ni₃(HATQ)₂ calculated from corresponding IFFT images in (a) using Digital Micrograph.
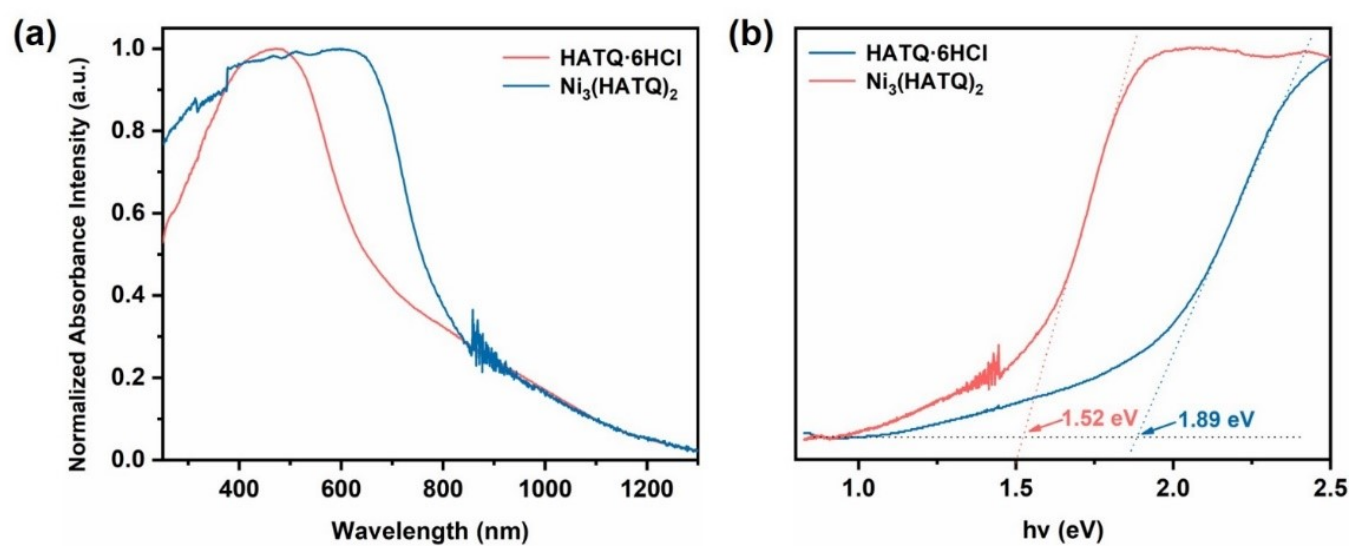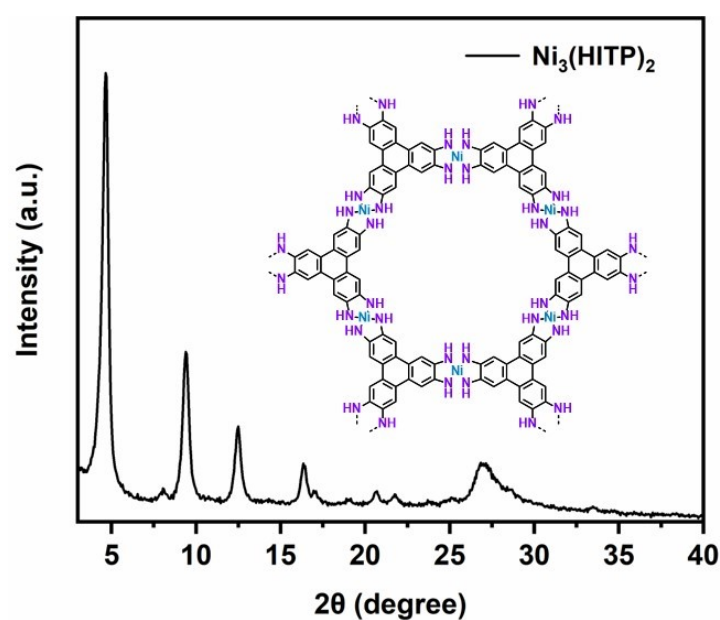
Fig. S17 (a) UV-visible diffuse reflectance spectra and (b) Kubelka-Munk-transformed reflectance spectra of HATQ·6HCl and Ni$_3$(HATQ)$_2$ in solid state.
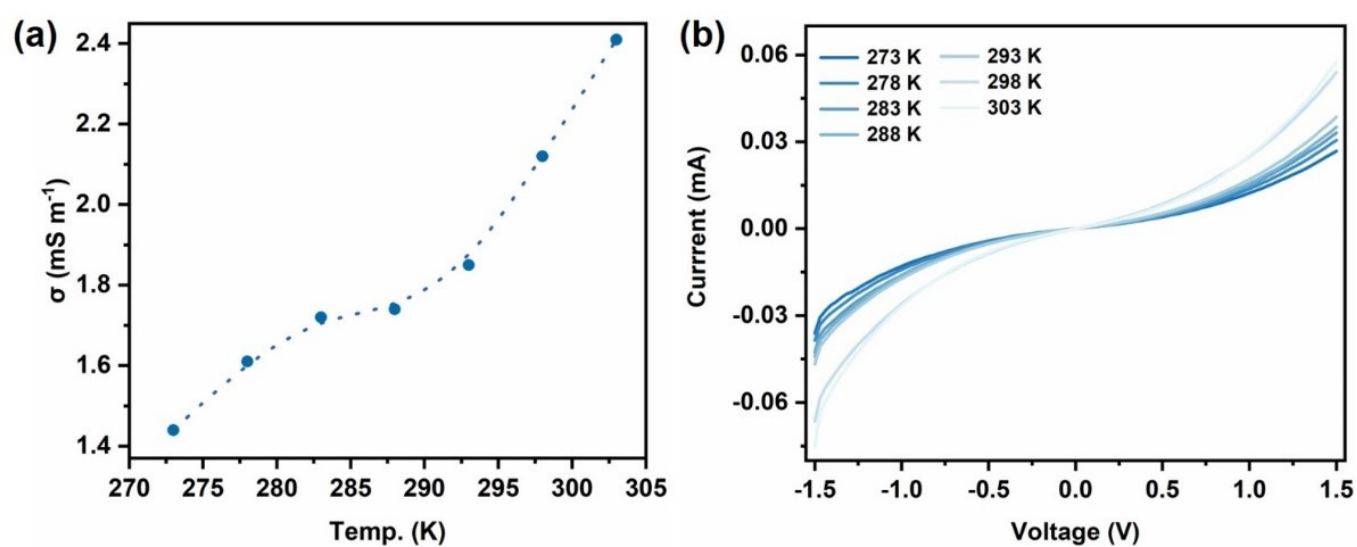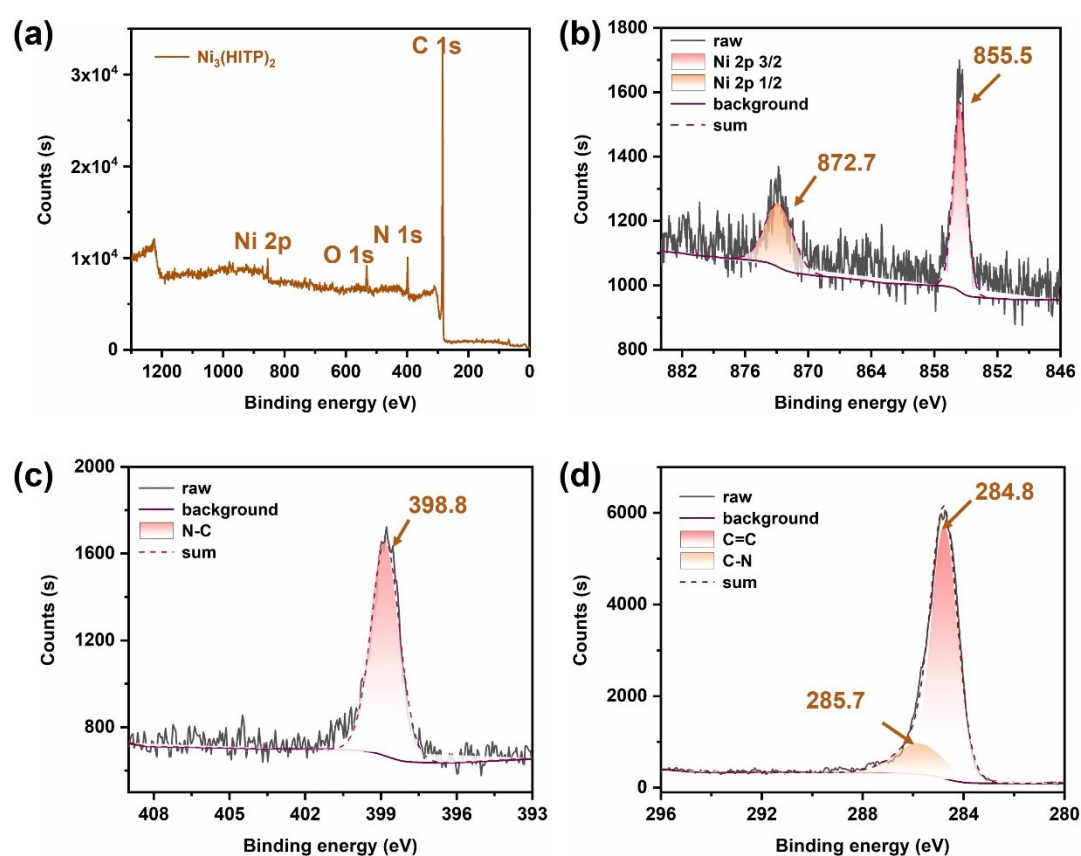

Fig. S18 Investigation on electronic conductivity of Ni$_3$(HATQ)$_2$ along with different temperature.
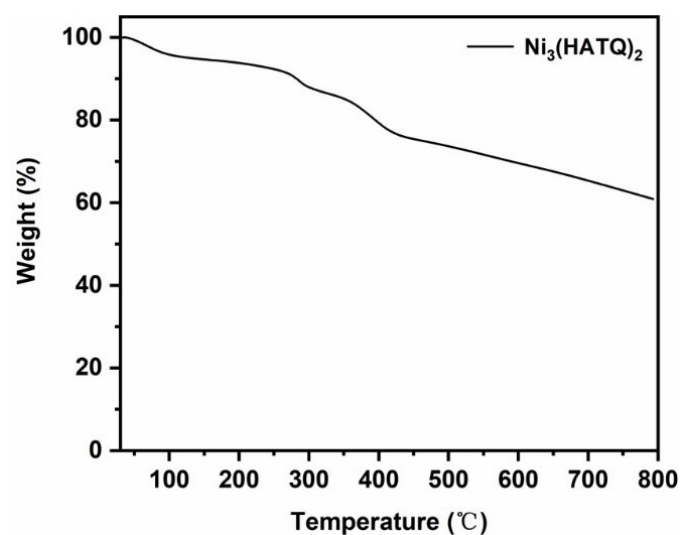
**Fig. S19** Thermogravimetric analysis (TGA) data of Ni$_3$(HATQ)$_2$ measured from room temperature to 800 ℃ at 10 ℃ min^{-1}.


Fig. S20 PXRD profiles of Ni$_3$(HITP)$_2$.

Fig. S21 (a) X-ray photoelectron spectroscopy (XPS) of full energy spectrum for all elements $Ni_3(HITP)_2$; (b) high resolution XPS Ni(2p) spectrum of $Ni_3(HITP)_2$; (c) high resolution XPS N(1s) spectrum of $Ni_3(HITP)_2$ and (d) high resolution XPS C(1s) spectrum of $Ni_3(HITP)_2$.

Section 6. Electrochemical Performance of $Ni_3(HATQ)_2$
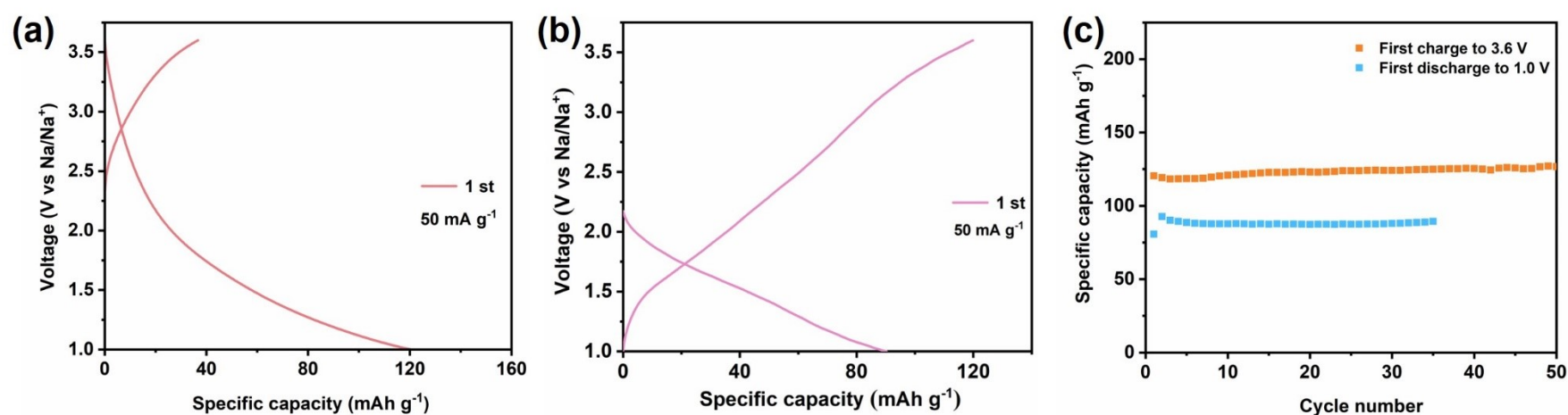
Fig. S22 GCD profiles of $Ni_3(HATQ)_2$-based cathode when charge to 3.6 V is conducted first (a) and discharge to 1.0 V is conducted first (b) in voltage range 1.0-3.6 V and (c) their corresponding cycling performance at 50 mA g^{-1}.
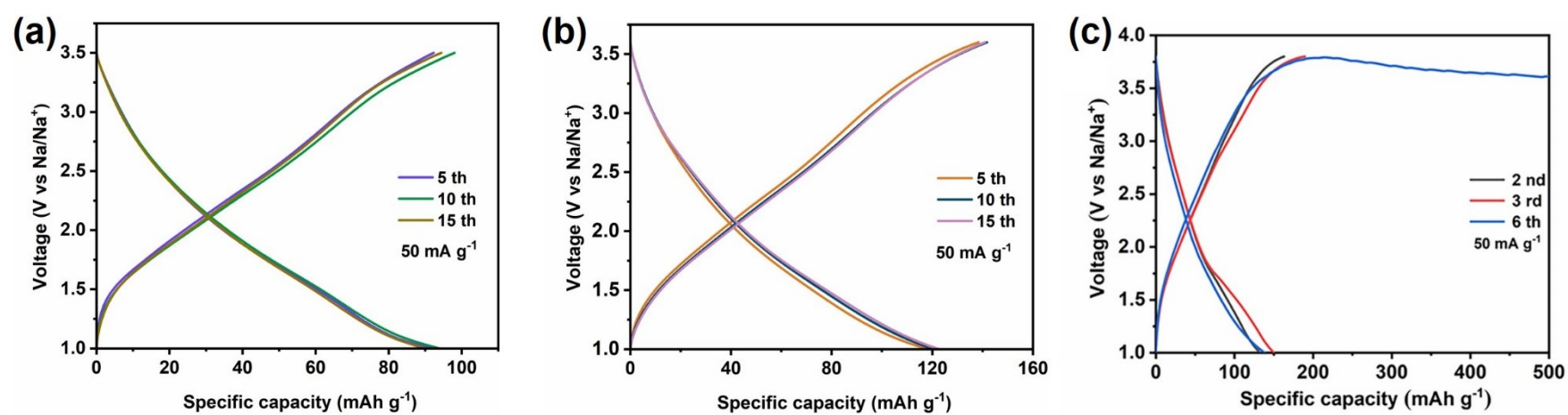
Fig. S23 GCD profiles of $Ni_3(HATQ)_2$-based cathode measured at (a) 1.0-3.5 V; (b) 1.0-3.6 V and (c) 1.0-3.8 V at 50 mA g^{-1}.
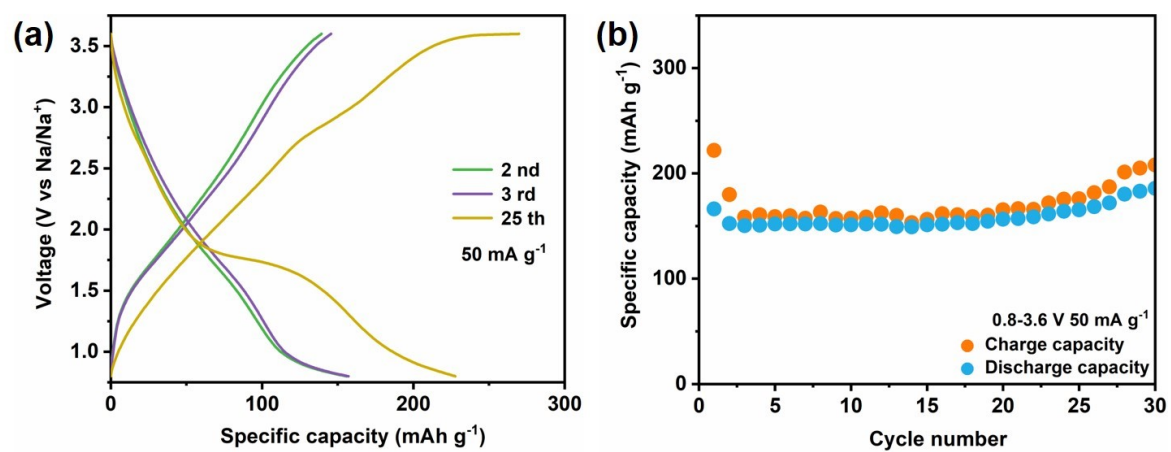
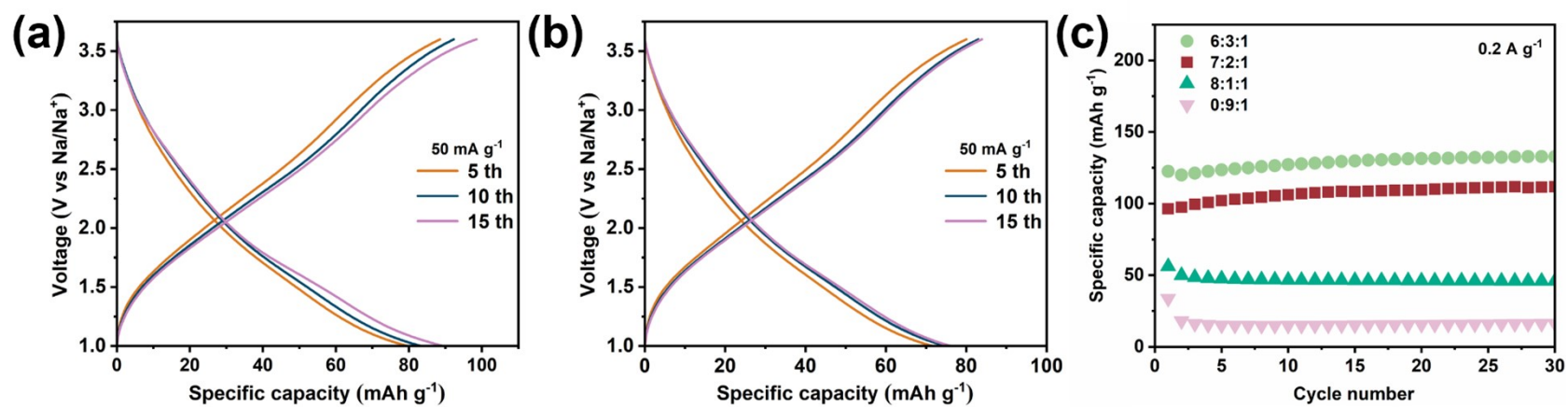**Fig. S24** (a) GCD profiles and (b) cycling performance of $Ni_3(HATQ)_2$ measured in voltage range of 0.8-3.6 V at 50 mA g^{-1}.

Fig. S25 GCD profiles of $Ni_3(HATQ)_2$ with different mass loading measured at 50 mA g^{-1} (a) 1.08 mg and (b) 1.44 mg; (c) long-term cycle performance of $Ni_3(HATQ)_2$-based electrode in different proportions measured at 0.2 A g^{-1}.
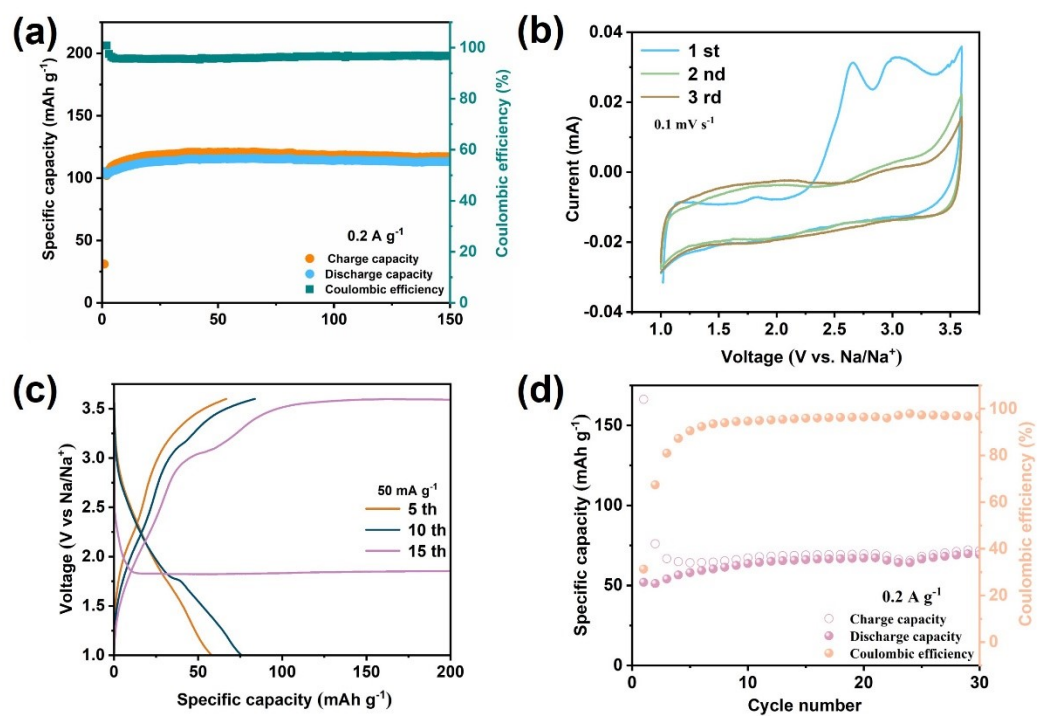

Fig. S26 (a) Cycling stability of $Ni_3(HATQ)_2$ at 0.2 A g^{-1}; (b) CV curves of HATQ·6HCl at 0.1 mV s-1; (c) GCD profiles of HATQ·6HCl-based cathode measured ranging from 1.0 V to 3.6 V at 50 mA g^{-1} and (d) the corresponding cycling performance at 0.2 A g^{-1}.

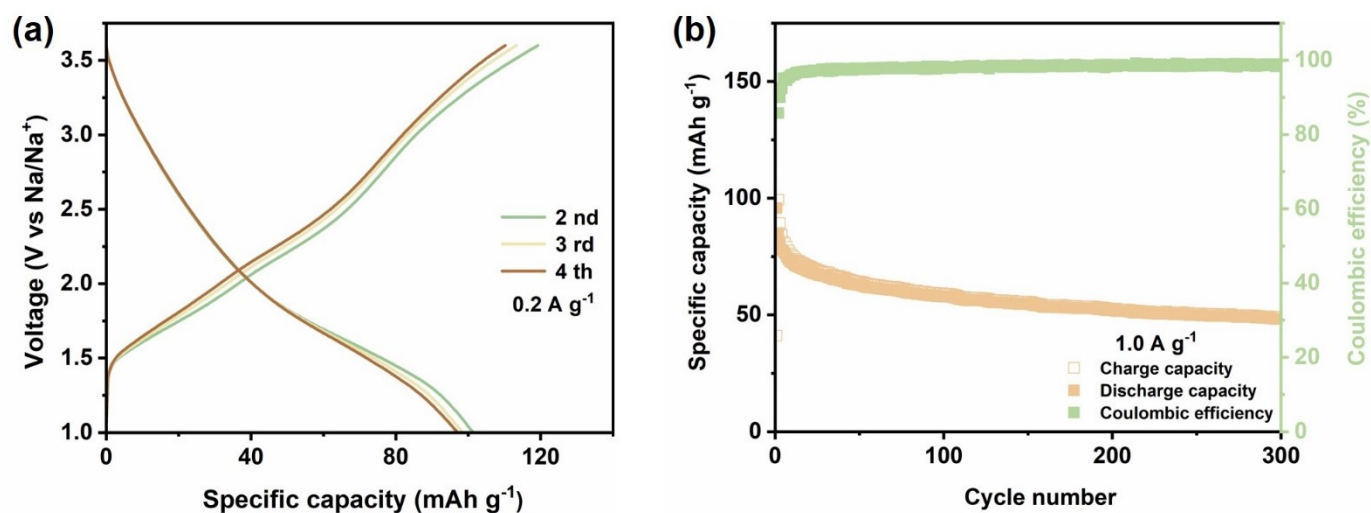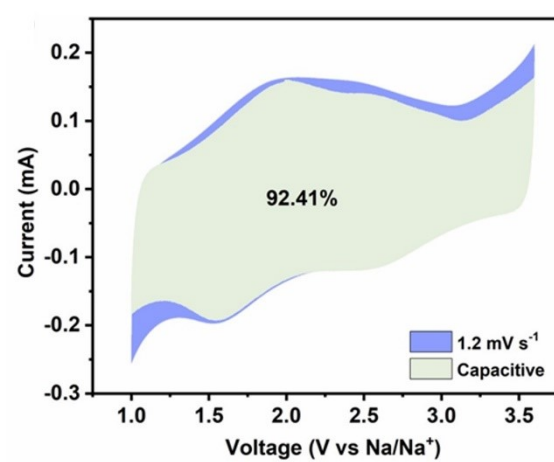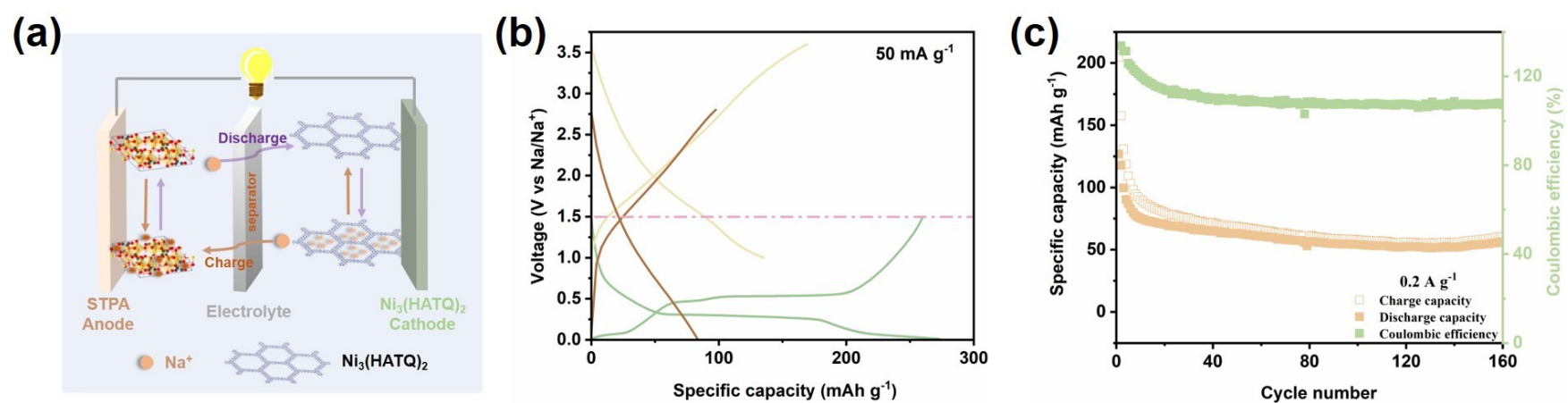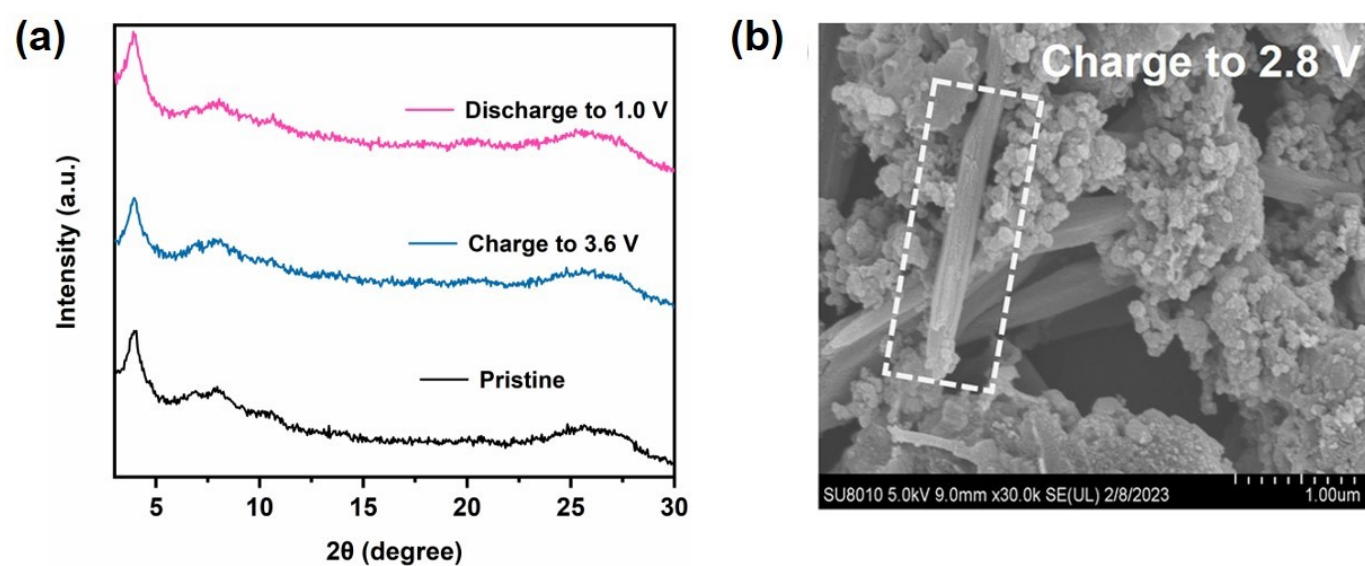**Fig. S27** (a) GCD profiles of $Ni_3(HITP)_2$ measured at 0.2 A $g^{-1}$and (b) the long cycle test of $Ni_3(HITP)_2$ measured at 1.0 A g^{-1}.

Fig. S28 Capacitive and diffusion-controlled contribution at 1.2 mV s^{-1}.

Fig. S29 (a) GCD profiles of Ni$_3$(HATQ)$_2$ measured at 50 mA g^{-1}and (b) the long cycle test of Ni$_3$(HATQ)$_2$ measured at 0.2 A g^{-1} when assembled into a full battery.

Fig. S30 (a) The *ex-situ* PXRD spectra of Ni$_3$(HATQ)$_2$-based cathode at different voltages of charge and discharge and (b) the SEM image of Ni$_3$(HATQ)$_2$ after charging to 2.8 V.
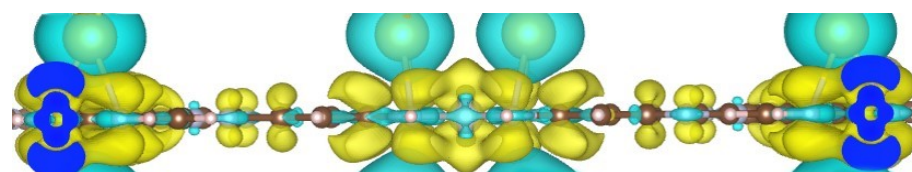
Fig. S31 The differential charge densities of Ni$_3$(HATQ)$_2$-Na from the side view

Table S2. Comparison of electrochemical performance between $Ni_3(HATQ)_2$ and MOFs/other inorganic cathodes for sodium-ion battery

Materials	Working voltage/ V	Current density/ mA g^{-1}	Capacity/ mAh g^{-1}	Reference
$Na_{0.7}CoO_2$	2.0–3.5	80	70.4	*Ceram. Int.* 2014, **40**, 2411–2417.
$Na_{2/3}Ni_{1/3}Mn_{2/3}O_2$	2.0–4.0	100	89	*J. Mater. Chem. A* 2019, **7,** 9215–9221.
$NaxMn_{0.5}Ni_{0.5}Fe(CN)_6$	2.0–4.0	150	100	*ACS Sustain. Chem. Eng.* 2022, **10**, 13277–13287
$NaCrO_2:Na_2NiO_2$	2.0–3.6	50	107.5	*Chem. Mater.* 2015, **27**, 6682–668
NaCoFe-PBA	2.0–4.1	100	106	*Electrochim. Acta* 2018, **272**, 44-51
NiCoFe-PBA	2.0–4.2	15	145	*Adv. Energy Mater.* 2018, **8**, 1702856.
ZIF-4(Co)	2.0–3.8	100	107.9	*J. Alloys Compd.* 2020, **815**, 152616.
NTP-rGO	1.5–3.0	100	129.2	*Nanoscale* 2019, **11**, 7347-7357.
$Zn_2(TTFTB)$	1.0–4.2	100	96	*ACS Appl. Energy Mater.* 2023, **6**, 9124−9135
Cu-TBA	1.0–3.5	100	130.0	*Adv. Mater.* 2024, 2401878. DOI:10.1002/adma.202401878
$Ni_3(HATQ)_2$	1.0–3.6	100	108.1	*This work*

Section 7. Supporting References

[S1] S. Xu, H. Li, Y. Chen, Y. Wu, C. Jiang, E. Wang and C. Wang, *J. Mater. Chem. A,* 2020, **8**, 23851-23856.

[S2] M. Yu, N. Chandrasekhar, R. K. M. Raghupathy, K. H. Ly, H. Zhang, E. Dmitrieva, C. Liang, X. Lu, T. D. Kühne, H. Mirhosseini, I. M. Weidinger and X. Feng, *J. Am. Chem. Soc.,* 2020, **142**, 19570-19578.

[S3] J. Wang, J. Polleux, J. Lim and B. Dunn, *J. Phys. Chem. C*, 2007, **111**, 14925-14931.

[S4] M. M. Cummings and B. C. G. Söderberg, *Synth. Commun.*, 2014, **44**, 954-958.

[S5] E. Keinan, S. Kumar, S. P. Singh, R. Ghirlando and E. J. Wachtel, *Liq. Cryst.*, 1992, **11**, 157-173.

[S6] S. Zhu, K. Shi, H. Zhu, Z.-K. Jia, X.-F. Xia, D. Wang and L.-H. Zou, *Org. Lett.*, 2020, **22**, 1504-1509.

[S7] L. Chen, J. Kim, T. Ishizuka, Y. Honsho, A. Saeki, S. Seki, H. Ihee and D. Jiang, *J. Am. Chem. Soc.*, 2009, **131**, 7287-7292.

[S8] T. Chen, J.-H. Dou, L. Yang, C. Sun, N. J. Libretto, G. Skorupskii, J. T. Miller and M. Dincă, *J. Am. Chem. Soc.*, 2020, **142**, 12367-12373.